

# Contents

<b>I</b>	<b>Measure ment of the jet transverse-momentum resolution</b>	<b>1</b>
<b>1</b>	<b>Introduction</b>	<b>3</b>
<b>2</b>	<b>General approach of the resolution measurement using photon+jet events</b>	<b>3</b>
2.1	The jet transverse-momentum response . . . . .	3
2.2	Basic concept of a data-based method . . . . .	5
<b>3</b>	<b>Datasets and event selection</b>	<b>6</b>
3.1	Datasets and triggers . . . . .	7
3.2	Simulated samples . . . . .	8
3.3	Event selection . . . . .	9
3.3.1	Jet selection . . . . .	9
3.3.2	Photon selection . . . . .	10
3.3.3	Photon+jet event selection . . . . .	11
<b>4</b>	<b>Methodology of the measurement</b>	<b>12</b>
4.1	Validation of the method . . . . .	18
<b>5</b>	<b>Systematic uncertainties</b>	<b>20</b>
<b>6</b>	<b>Results</b>	<b>25</b>
6.1	Comparison to 2011 measurements . . . . .	29
6.2	Comparison to dijet measurement . . . . .	30
<b>7</b>	<b>Discussion and conclusion</b>	<b>31</b>
<b>A</b>	<b>Measurement of the jet transverse momentum resolution</b>	<b>33</b>
A.1	Pileup reweighting . . . . .	33
A.2	Summary of all selection requirements . . . . .	34
A.3	Generator-level jet flavor definition . . . . .	34
A.4	Extrapolation plots . . . . .	35



## **Part I**

### **Measurement of the jet transverse-momentum resolution**



# 1 Introduction

The determination and quantification of the quality of the jet transverse-momentum measurement is of crucial interest for many analyses with jet final states, e. g. the measurement of the dijet cross section [1] or  $t\bar{t}$  production cross sections [2]. Also searches for physics beyond the standard model with missing transverse momentum,  $\cancel{p}_T$ , in the final state need a good knowledge of  $\cancel{p}_T$  originating from wrongly measured jets [3–5]. For analyses relying on information from simulation it is very important to correct the simulated resolution to the resolution actually present in data. Therefore, scale factors will be presented to adjust the resolution in simulation to the resolution of the real detector.

In the following sections, a data-based method to measure the jet  $p_T$  resolution in  $\gamma + \text{jet}$  events will be presented. A similar method was already accomplished in earlier analyses [6, 7] of 7 TeV data. It is further developed here and applied to  $19.7 \text{ fb}^{-1}$  of 8 TeV data.

The method is based on the transverse-momentum balance in the  $\gamma + \text{jet}$  system. It takes advantage of the high resolution of the electromagnetic calorimeter and hence the excellent measurement of the photon energy and momentum. Without initial and final state radiation, the photon and the jet are balanced in the transverse plane. Thus, measuring the photon  $p_T$  with high accuracy leads to an estimate of the true jet transverse momentum offering a possibility to quantify the resolution of jet  $p_T$  measurements.

## 2 General approach of the resolution measurement using photon+jet events

### 2.1 The jet transverse-momentum response

The jet transverse-momentum resolution is defined as the standard deviation of the jet transverse-momentum response distribution with the response defined as the ratio of the

reconstructed to the generator-level jet transverse momentum

$$\mathcal{R} = \frac{p_{\text{T}}^{\text{reco. jet}}}{p_{\text{T}}^{\text{gen. jet}}}. \quad (2.1)$$

For each reconstructed jet, the underlying generator-level jet is hereby found by matching the closest generator-level jet to the reconstructed jet with  $\Delta R = \sqrt{(\Delta\phi)^2 + (\Delta\eta)^2}$  with a maximal value of  $\Delta R_{\text{max}} = 0.25$ . Furthermore, the transverse momentum of the generator-level jet is defined as the sum of all particles' transverse momenta from the hadronisation that are clustered into the jet cone. Throughout the following sections, the jet transverse-momentum resolution will be abbreviated JER<sup>1</sup>. The mean of the response distribution will be referred to as jet energy scale.

Figure 2.1 shows a response distribution for jets in the barrel region. The core of the response distribution shows the typical Gaussian behaviour whereas the tails deviate from that functional form. Physical reasons for the low response tail are inter alia semi-leptonic decays of heavy quarks where the neutrino cannot be detected and the reconstructed transverse momentum of the jet is too small. This effect is visible in Fig. 2.1 because the neutrinos are included into the generator-level jet. Some instrumental effects, such as a non-linear response of the calorimeter, inhomogeneities of the detector material and electronic noise can contribute to both tails, others, like dead calorimeter channels only

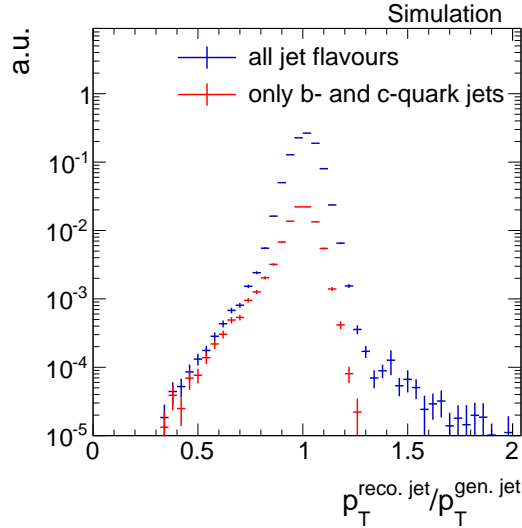


Figure 2.1: Number of events over  $p_{\text{T}}^{\text{reco. jet}}/p_{\text{T}}^{\text{gen. jet}}$  from a simulated  $\gamma + \text{jet}$  sample. The black dots show the contribution by c- and b-quark jets which cause almost fully the left tail originating from semi-leptonic decays.

<sup>1</sup>This abbreviation is a historical relic from experiments where the momentum of jets were only measured in the calorimeters and therefore JER referred to jet energy resolution.

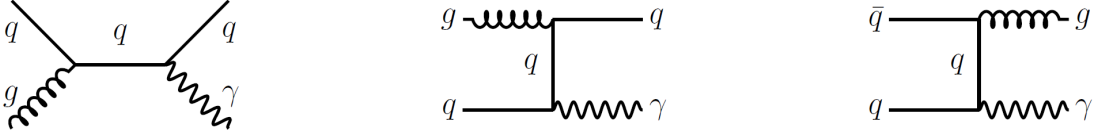


Figure 2.2: Tree-level Feynman diagrams of processes at the LHC in pp collisions with one photon and one jet in the final state.

contribute to the left tail. The resolution is therefore determined using only the core of the distribution to avoid the coverage of non-Gaussian tails. The resolution is thus defined as the standard deviation of the 99% truncated response histogram divided by the mean of the histogram:

$$\sigma_{\text{JER}} = \frac{\sigma_{99\%}}{\mu_{99\%}}.$$

The determination of the 99% range of the histogram is done in several steps. First the mean of the core is found via a Gaussian fit to the histogram in a  $2\sigma$  range<sup>2</sup>. This procedure is done in three iteration steps. Then, a symmetric interval around this mean is determined with its integral equal to 99% of the integral of the full histogram. The division by the mean aims to make the resolution independent of the absolute scale (= mean) of the response distribution. It is done because response distributions with a scale smaller than one are typically narrower while distributions with scales larger than one are broader. However, since after the application of the jet energy corrections the scale is very close to one, this is only a tiny effect.

The evaluation of the response distribution as reconstructed over generator-level jet transverse momentum (Eq. (2.1)) is only possible for simulated events where generator-level information is accessible. A determination of the resolution in data, however, has to rely on a different approach.

## 2.2 Basic concept of a data-based method

The main idea of a resolution measurement using  $\gamma$ +jet events is based on the transverse-momentum balance of the  $\gamma$ +jet system and the excellent electromagnetic calorimeter resolution (which was estimated between 1.4% and 3.8% in the barrel region for photons for  $\sqrt{s} = 8$  TeV data [8]).

In Fig 2.2, all tree-level processes contributing to an event topology with one photon and one jet in the final state are depicted. Due to momentum conservation, the jet and

<sup>2</sup>The  $2\sigma$  range is defined as the range  $[\mu - 2\sigma, \mu + 2\sigma]$ .

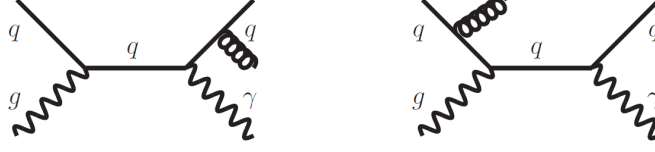


Figure 2.3: Tree-level Feynman diagrams with initial and final state radiation.

the photon are back to back in the transverse plane, and therefore,  $\vec{p}^\gamma = -\vec{p}^{\text{jet}}$ . Because of the good resolution of the electromagnetic calorimeter, photon momenta can be very well measured and thus can serve as an excellent estimator for the true jet momentum.

Unfortunately, such clean events are very rare processes, and usually, the momentum balance is spoiled by initial and final state radiation, which lead to further jets in the event (see Fig. 2.3). However, in order to select events that are balanced to a large extent, a lower bound on the angular distance in the transverse plane between the photon and the jet with the highest transverse momentum (leading jet) is required:  $\Delta\Phi(1^{\text{st}} \text{ jet}, \gamma) > 2.95 \text{ rad}$ .

Additionally, the variable

$$\alpha \doteq \frac{p_{\text{T}}^{2^{\text{nd}} \text{ reco. jet}}}{p_{\text{T}}^\gamma}$$

is defined as a measure of further jet activity in an event. It is, however, not sufficient to require only an upper bound on  $\alpha$ . Instead, the jet transverse-momentum resolution is measured in bins of  $\alpha$  (with  $\max(\alpha) = 0.2$ ), and the extrapolated value to zero further jet  $p_{\text{T}}$  ( $\alpha = 0$ ) is taken as the measured resolution of the jet  $p_{\text{T}}$  in the absence of further jets.

Measuring the transverse momentum of the photon instead of taking the generator-level jet  $p_{\text{T}}$  leads to the fact that the measured resolution consists out of two parts

$$\frac{p_{\text{T}}^{\text{reco. jet}}}{p_{\text{T}}^\gamma} = \underbrace{\frac{p_{\text{T}}^{\text{reco. jet}}}{p_{\text{T}}^{\text{gen. jet}}}}_{\text{intrinsic}} \cdot \underbrace{\frac{p_{\text{T}}^{\text{gen. jet}}}{p_{\text{T}}^\gamma}}_{\text{imbalance}}.$$

The intrinsic part is the resolution of interest which is independent of further jets in the event whereas the imbalance is strongly dependent on  $\alpha$ .

To extract the intrinsic resolution out of the measured one, the residual imbalance  $q$  (the imbalance at  $\alpha = 0$ ) is subtracted from the total resolution in the limit of vanishing additional jet activity. As that information is only available from simulation, the measured resolution in data is corrected by the residual imbalance taken from the simulated dataset.

To account for differences in the jet transverse-momentum resolution for different true jet  $p_{\text{T}}$  and different jet pseudorapidity regions, the measurement of the resolution is done in  $p_{\text{T}}^\gamma$  bins and bins of  $|\eta|$  of the leading jet.



## 3 Datasets and event selection

The measurement of the jet transverse-momentum resolution is carried out with  $\gamma + \text{jet}$  data recorded during the year 2012 at the CMS experiment. The datasets and triggers that are exploited for this measurement are introduced in the following Section 3.1. In order to select  $\gamma + \text{jet}$  events that are well suited for the resolution measurement, an event selection is applied on top. This event selection is described in Section 3.3.

### 3.1 Datasets and triggers

This analysis exploits several triggers which were active during the year 2012 at the CMS experiment. Because of the high production cross section of  $\gamma + \text{jet}$  events, especially for low photon  $p_T$ , almost all of these triggers were highly prescaled, i. e. only a fraction of events were actually recorded when the triggers fired. All triggers that are utilised in this measurement are listed in Table 3.1 together with their recorded luminosity. The triggers rely on level one on single-photon triggers, such as L1SingleEG12 and L1SingleEG30. The L1 triggers require at least one photon that is above a certain  $p_T$  threshold, e. g. 12 GeV

Table 3.1: Single-photon triggers together with the recorded luminosity taking the prescales of the triggers into consideration.

Trigger	Luminosity [ $\text{fb}^{-1}$ ]
HLT_Photon20_CaloIdVL_IsoL	0.0008
HLT_Photon30_CaloIdVL_IsoL	0.0029
HLT_Photon50_CaloIdVL_IsoL	0.0607
HLT_Photon75_CaloIdVL_IsoL	0.123
HLT_Photon90_CaloIdVL_IsoL	0.373
HLT_Photon135	13.77
HLT_Photon150	19.71

or 30 GeV. The high-level triggers require a photon with a certain  $p_T$  (as indicated in the name) and, in case of thresholds below 135 GeV also additional quality and isolation criteria. All triggers with threshold below 150 GeV were prescaled.

The events that are selected by the above mentioned triggers are contained in the datasets listed in Table 3.2.

Table 3.2: Single-photon data samples used for the resolution measurement with the contained integrated luminosity.

Dataset	Luminosity [ $\text{fb}^{-1}$ ]
/Photon/Run2012A-22Jan2013-v1/AOD	0.876
/SinglePhoton/Run2012B-22Jan2013-v1/AOD	4.412
/SinglePhoton/Run2012C-22Jan2013-v1/AOD	7.055
/SinglePhotonParked/Run2012D-22Jan2013-v1/AOD	7.354

## 3.2 Simulated samples

In order to compare the measured resolution in data to the resolution in simulation, a single-photon sample simulated with PYTHIA6 is used. This sample was generated flat in the photon  $p_T$  to have a good statistical precision also for the high photon  $p_T$  region. In order to recover a physical  $p_T$  spectrum, all simulated events are reweighted. Figure 3.1 shows the photon  $p_T$  spectrum in simulation before and after the reweighting.

All simulated samples come with a pileup scenario which does not necessarily match the pileup scenario in data. To match the measured distribution of primary vertices, the events are weighted according to their number of primary vertices. Because almost all of the used triggers are differently prescaled, the distributions of primary vertices differ among the various events triggered by the corresponding trigger. Thus the reweighting has to be done separately for the events falling in the photon  $p_T$  range of the several triggers (see Table 3.3). A comparison between the number of primary vertices can be found in Appendix A.1 for all triggers.

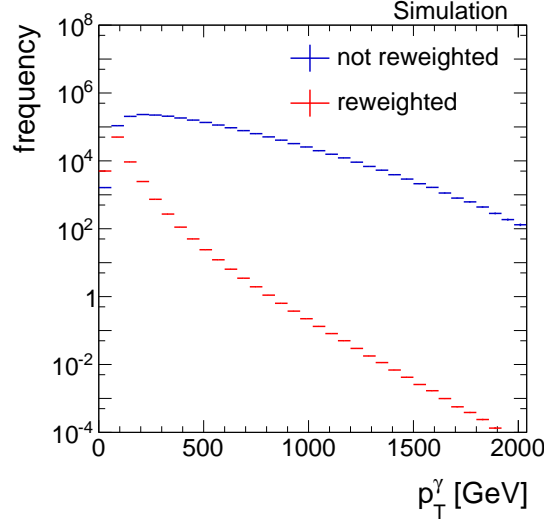


Figure 3.1: The photon  $p_T$  spectrum before (blue) and after (red) reweighting.

### 3.3 Event selection

Events are reconstructed with the particle-flow reconstruction algorithm, which uses information of all detector components to reconstruct individual particles [9]. In the following, the selection of well reconstructed jets and photons will be explained as well as the event selection of  $\gamma + \text{jet}$  events.

#### 3.3.1 Jet selection

Furthermore, particles belonging to a jet are clustered with the Anti- $k_t$  jet clustering algorithm with a radius of  $R=0.5$  [10].

To select clean  $\gamma + \text{jet}$  events, it is required that the leading jet meets the following requirements (these criteria correspond to a 'tight ID' in [11, 12]):

- Neutral hadron fraction  $< 0.90$
- Neutral electromagnetic fraction  $< 0.90$
- Number of constituents  $> 1$

And for jets in the pseudorapidity range  $|\eta| < 2.4$ :

- Charged hadron fraction  $> 0$
- Charged hadron multiplicity  $> 0$
- Charged electromagnetic fraction  $< 0.99$

These selection cuts ensure a selection efficiency of around 99% and a noise rejection efficiency of 99.98% [11]. To mitigate effects from pileup, the first and second jet are required to have a transverse momentum greater 10 GeV.

### 3.3.2 Photon selection

Concerning the photon, a maximal pseudorapidity of the photon of  $|\eta^\gamma| < 1.3$  is demanded to exploit the high resolution of the ECAL in the barrel region.

Furthermore, the resolution is determined for different ranges in photon  $p_T$  to avoid mixing of different prescales of the various triggers. In Table 3.3 the applied binning is shown with the respective triggers contributing to each  $p_T^\gamma$  bin.

Table 3.3: Photon  $p_T$  bins and corresponding triggers.

$p_T^\gamma$ -bins	Trigger
22 GeV	HLT_Photon20_CaloIdVL_IsoL_v*
36 GeV	HLT_Photon30_CaloIdVL_IsoL_v*
60 GeV	HLT_Photon50_CaloIdVL_IsoL_v*
88 GeV	HLT_Photon75_CaloIdVL_IsoL_v*
105 GeV	HLT_Photon90_CaloIdVL_IsoL_v*
149 GeV	HLT_Photon135_v*
165 GeV	HLT_Photon150_v*

QCD-multijet events constitute an important background to the  $\gamma$ +jet events: A photon can be faked by a  $\pi^0$  decaying into two close-by photons. Therefore, a very clean selection of the photons is necessary to suppress this background. The following variables are used (see [13] for further explanation of the variables):

- $\frac{H}{E}$  : The ratio of the measured energy in the hadronic calorimeter over the energy measured in the electromagnetic calorimeter. For photons, this is supposed to be very small as they deposit their energy predominantly in the ECAL.
- $\sigma_{i\eta i\eta}$ : The energy weighted spatial width of the photon energy deposition. The electromagnetic shower of a photon has a small lateral size resulting in small  $\sigma_{i\eta i\eta}$  for prompt photons while showers from fake photons, e.g.  $\pi^0 \rightarrow \gamma\gamma$  have a larger lateral size.

- **Jurassic ECAL isolation:** This isolation criterion uses the information of reconstructed hits “RecHits” (coming from the local reconstruction of the digital signals) in a cone around the photon supercluster of  $R=0.4$ . Those are summed up and an upper criterion is identified to discriminate against background which is typically spatially broader.
- **Tower-based HCAL isolation:** The isolation criterion requires the energy deposited in all HCAL towers around the photon in cone of  $R=0.4$  to be small compared to the photon’s energy.
- **Hollow cone track isolation:** Requires absence of high-energetic tracks around the photon.
- **Pixel seed veto:** In order to reduce the background from electrons and positrons, the absence of a pixel-seed in the pixel tracker along the photons trajectory is required.

The upper and lower bounds that are set on these observables can be found in Table 3.4.

Table 3.4: Upper and lower bounds for all photon isolation criteria in the barrel ( $|\eta^\gamma| < 1.4442$ ).

Barrel	
$\frac{H}{E}$	$< 0.05$
$\sigma_{i\eta i\eta}$	$< 0.013$
ECAL isolation	$< 4.2 \text{ GeV} + 0.0060 \cdot p_T^\gamma$
HCAL isolation	$< 2.2 \text{ GeV} + 0.0025 \cdot p_T^\gamma$
Track Isolation	$< 2.0 \text{ GeV} + 0.0010 \cdot p_T^\gamma$
Pixel seed veto	yes

### 3.3.3 Photon+jet event selection

Besides the mentioned requirements concerning the objects’ attributes, two further criteria related to the event topology are crucial for this analysis:

An upper threshold on  $\Delta\Phi$  between the leading jet and the photon and a maximal value for  $\alpha$

- $\Delta\Phi(1^{\text{st}} \text{ jet}, \gamma) > 2.95 \text{ rad}$
- $\frac{p_{\text{T}}^{2^{\text{nd}} \text{ jet}}}{p_{\text{T}}^{\gamma}} < 0.20$ .

These requirements are important to suppress events with too much further hadronic activity.

A summary of all selection criteria can be found in Appendix A.2.

## 4 Methodology of the measurement

The basic methodology of measuring the jet transverse-momentum resolution by exploiting the  $p_{\text{T}}$  balance in  $\gamma + \text{jet}$  events and extrapolating the result to small  $\alpha$ , that was already used in earlier analyses [6, 7], is extended in this measurement in order to explicitly distinguish the case of parton radiation in different event hemispheres.

As already described in Chapter 2, the idea behind a resolution measurement with  $\gamma + \text{jet}$  events is the usage of the photon  $p_{\text{T}}$  instead of the true jet  $p_{\text{T}}$ . This results in a twofold contribution to the measured response, the intrinsic response and the imbalance:

$$\frac{p_{\text{T}}^{\text{reco. jet}}}{p_{\text{T}}^{\gamma}} = \underbrace{\frac{p_{\text{T}}^{\text{reco. jet}}}{p_{\text{T}}^{\text{gen. jet}}}}_{\text{intrinsic}} \cdot \underbrace{\frac{p_{\text{T}}^{\text{gen. jet}}}{p_{\text{T}}^{\gamma}}}_{\text{imbalance}}. \quad (4.1)$$

Taking the photon  $p_{\text{T}}$  as true jet  $p_{\text{T}}$  estimator instead of the generator jet  $p_{\text{T}}$ , and thus measuring the response defined as  $p_{\text{T}}^{\text{reco. jet}}/p_{\text{T}}^{\gamma}$ , results in a different shape of the response function as shown in Fig. 4.1. The figure compares the intrinsic response, the imbalance, and the measured total response in simulation.

The clear difference between the intrinsic response and the imbalance is the double peak structure of the latter one. The measured response is a convolution of the two contributions, where the double peak is consequentially less pronounced.

The occurrence of two peaks is caused by the hard selection in  $\Delta\phi$  which forces the second jet to be either close to the photon or close to the leading jet due to  $p_{\text{T}}$  conservation. The possibility of an energetic second jet perpendicular to the leading jet-photon axis which is balanced by a third jet is very unlikely due to the decreasing jet multiplicity in QCD-multijet events. The double peak structure is less pronounced for small second jet

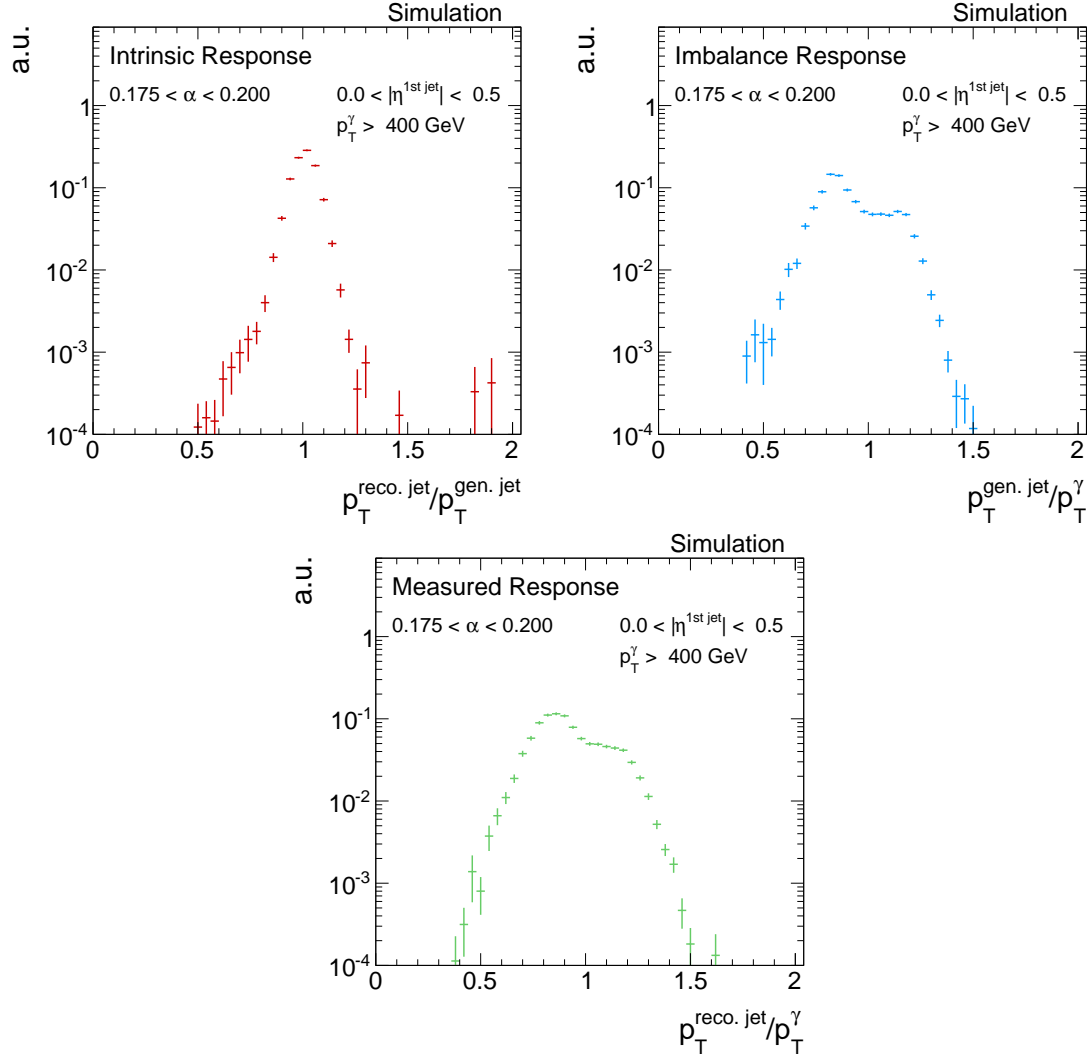


Figure 4.1: The two different contributions, intrinsic (top left) and imbalance (top right), to the measured response (bottom) (cf. Eq. (4.1)) in simulated events.

$p_T$  (small  $\alpha$ ) where the  $\Delta\Phi$  requirement does not have such a strong effect in rejecting events with a second jet perpendicular to the photon leading jet axis (see Fig. 4.2).

These two different contributions (second jet in photon/leading jet hemisphere) result in two separate response distribution. A schematic sketch of the two contributions is shown in Fig. 4.3.

The mathematical definitions of the hemispheres are as follows:

$$\text{Hemisphere} = \begin{cases} \text{Jet}, & \Delta\Phi(1^{\text{st jet}}, 2^{\text{nd jet}}) < \Delta\Phi(\gamma, 2^{\text{nd jet}}), \\ \text{Photon}, & \text{else.} \end{cases} \quad (4.2)$$

The two response distributions coming from the different event topologies are separately

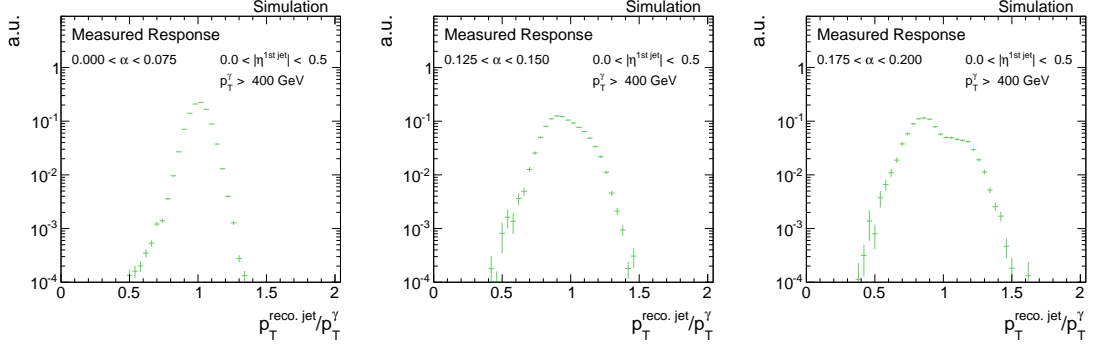


Figure 4.2: The measured response  $p_T^{\text{reco. jet}}/p_T^\gamma$  in simulation for FIXME :  $p_T^\gamma < 400$  GeV for three different  $\alpha$  ranges: 0.0 – 7.5% (left), 12.5 – 15.0% (middle) and 17.5 – 20.0% (right). It can be seen that the double peak structure gets less pronounced for low  $\alpha$  values.

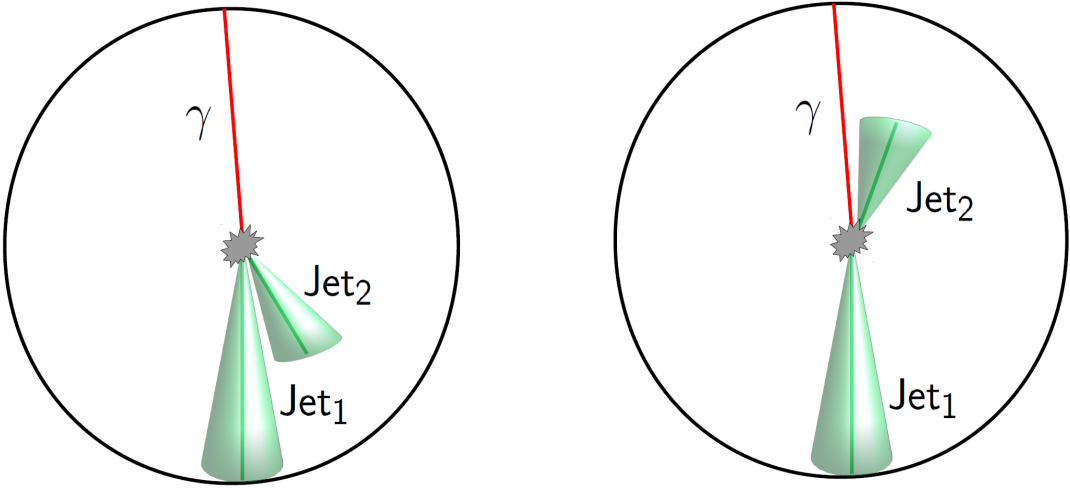


Figure 4.3: A schematic sketch of the two different event topologies where the second jet is in the leading jet (left) or the photon hemisphere (right)

evaluated. First, the resolution is determined for each of the configurations (cf. Fig. 4.4), and then, the weighted mean of the two contributions is calculated.

As can be seen in Fig. 4.4, events containing a second jet in the leading jet hemisphere lead to a response histogram with mean smaller one, while events with a second jet in photon direction result in a distribution with mean larger one. The former occurs more frequently because it contains jets from final and initial state radiation, while the latter mainly consists only from initial state radiation.

The intrinsic part of the resolution for a given photon  $p_T$  bin is independent of secondary



jet  $p_T$  and thus can be considered as constant in terms of  $\alpha$

$$\sigma_{\text{intrinsic}}(\alpha) = c. \quad (4.3)$$

This is not true for the imbalance part. It was found empirically that the  $\alpha$  dependence of the imbalance can be described by a linear function

$$\sigma_{\text{imbalance}}(\alpha) = q + m \cdot \alpha \quad (4.4)$$

Folding two independent Gaussian functions results in a quadratic addition of the corresponding standard deviations  $\sigma_{\text{intr.}} \oplus \sigma_{\text{imb.}}$ .

$$\sigma_{\text{total}}(\alpha) = \sqrt{c^2 + q^2 + 2q m \cdot \alpha + m^2 \cdot \alpha^2}. \quad (4.5)$$

In Fig. 4.5, the  $\alpha$  dependence of the imbalance, the intrinsic resolution, and the total resolution is shown for two exemplary  $p_T^\gamma$  regions in simulated events. The measured intrinsic resolution and imbalance for various  $\alpha$  values are fitted with functions (4.3) and (4.4), respectively. The measured total resolution (black dots) is fitted with function (4.5). Here, only  $c$  and  $m$  are free parameters, whereas  $q$  is fixed to the value obtained from the imbalance fit. All contributions are well described by their fit functions. The grey line is

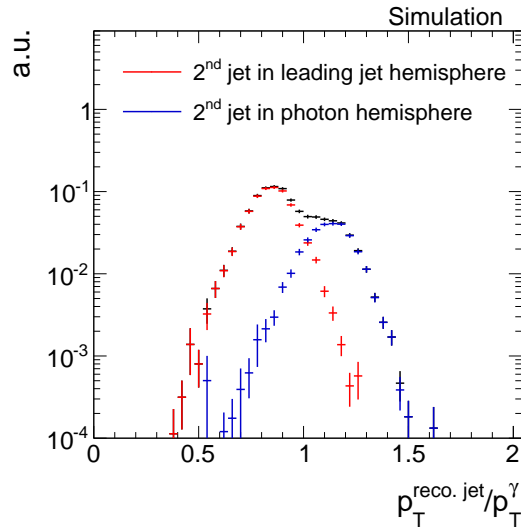


Figure 4.4: The measured response with the two contributions visualised. Events with a second jet in photon hemisphere (red) lead to a mean response larger one, while events with a second jet in the leading jet hemisphere (green) have a mean smaller one.

the total resolution with the analytic expression of function (4.5) with the parameters set to the fit values of the intrinsic and the imbalance fit.

It is apparent that the imbalance is not zero for  $\alpha = 0$ . This has two reasons. First and most important, only the photon and the parton are balanced in the transverse plane. But since the transverse momentum of a jet is defined as the sum of all particles' transverse momenta that are clustered into the jet cone, the jet  $p_T$  can be lower than the  $p_T$  of the original parton. This effect is called out-of-cone showering and leads to a residual imbalance between the photon  $p_T$  and the generator-level jet  $p_T$  at  $\alpha = 0$ . Second, also the photon  $p_T$  can be wrongly measured and spoil the residual imbalance  $q$ .

These two effects lead to a small discrepancy between the measured resolution (black) and the intrinsic resolution (red) also for zero second jet  $p_T$ . To correct for this effect,  $q$  is fixed to the value obtained from fitting the imbalance part of the resolution (Eq. (4.4)) and then only the fit parameter  $c$  is taken as the relevant resolution from the fit. Also for measured data,  $q$  is fixed to the value obtained from simulation. Figure 4.6 shows the residual imbalance for two exemplary  $|\eta^{1\text{st jet}}|$  bins. It is almost stable and around 2% over the whole photon  $p_T$  range.

In Fig. 4.7, the fitted intrinsic resolution in simulation is shown in the different photon  $p_T$  bins for two different  $|\eta^{1\text{st jet}}|$  regions. The resolution improves for increasing photon  $p_T$ . For the  $|\eta^{1\text{st jet}}| < 0.5$  region, the resolution is approximately 10% for  $p_T^\gamma \approx 100$  GeV and decreases to values around 6% for  $p_T^\gamma \approx 500$  GeV. The increasing statistical uncertainties

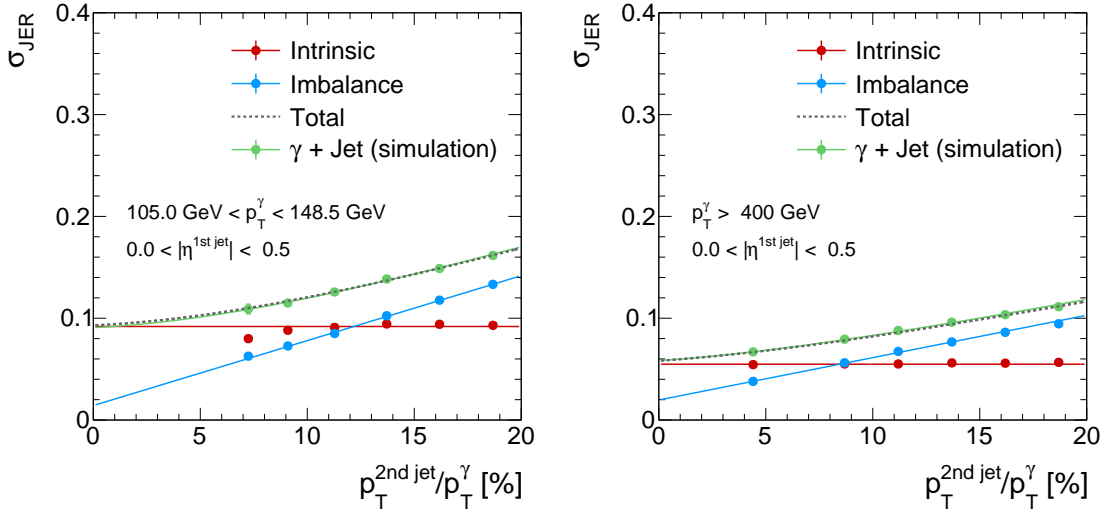


Figure 4.5: The alpha dependency of the various parts of the resolution in the simulated events for  $83 \text{ GeV} < p_T^\gamma < 99 \text{ GeV}$  (left) and  $400 \text{ GeV} < p_T^\gamma$  (right). The total resolution (grey dotted line) is the addition in quadrature of the imbalance (blue line) and the intrinsic (red line) fit functions. It can be compared to the measured pseudo data (green dots/line).

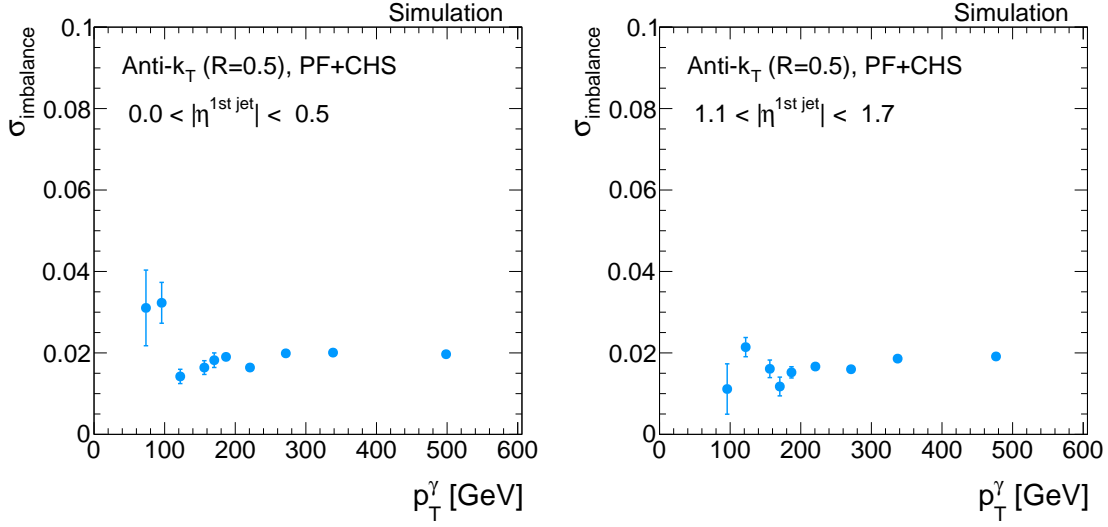


Figure 4.6: Imbalance for  $|\eta^{1\text{st jet}}| < 0.5$  (left) and  $1.1 < |\eta^{1\text{st jet}}| < 1.7$  (right) in simulation.

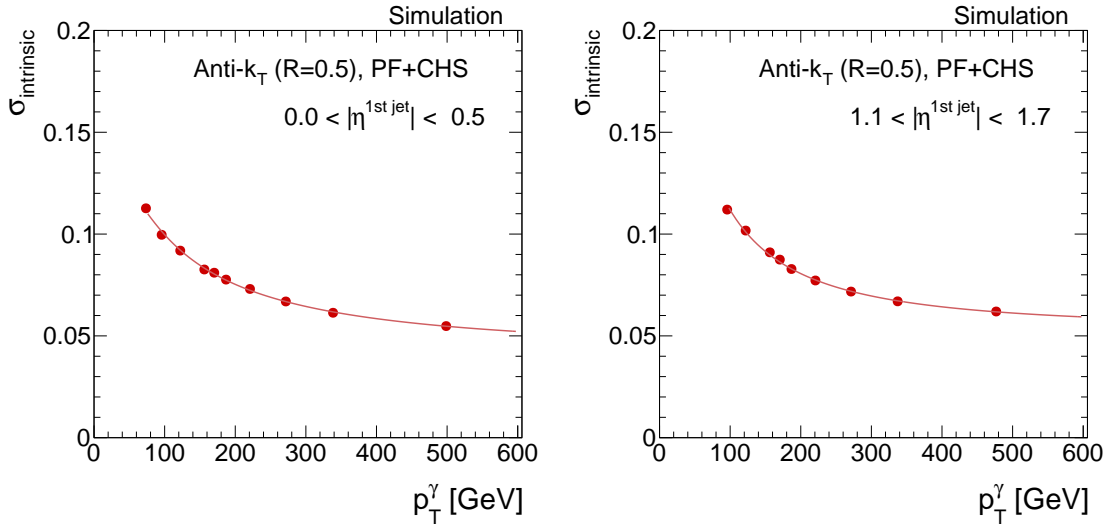


Figure 4.7: Intrinsic resolution for  $|\eta^{1\text{st jet}}| < 0.5$  (left) and  $1.1 < |\eta^{1\text{st jet}}| < 1.7$  (right) in simulation.

for low photon  $p_T$  arise through the requirement of a maximal  $\alpha$  and a minimal  $p_T$  of the second jet. This reduces the numbers of events in the low photon  $p_T$  bins. For events with  $p_T^\gamma \lesssim 50$  GeV, it is not possible at all to fulfil both requirements at the same time.

The extrapolated intrinsic resolutions for the various photon  $p_T$  are fitted with the following function

$$\sigma_{\text{JER}} = \sqrt{\text{sgn}(N) \cdot \frac{N}{p_T} + S^2 \cdot p_T^{M-1} + C^2} \quad (4.6)$$

which was introduced for particle flow jets in [6]. It is an extended fit function compared to the usual calorimeter resolution parametrisation to account for the higher resolution due to tracking information.

Finally, in order to measure data-to-simulation scaling factors  $\rho_{\text{res}}$  for the jet transverse-momentum resolution, the measured resolution in data is divided by the resolution in simulation

$$\rho_{\text{res}} = \frac{\sigma^{\text{data}}}{\sigma^{\text{MC}}} \quad (4.7)$$

It was found empirically, that this ratio is independent of  $p_T^\gamma$ , and can be fitted with a constant. Thus, to account for differences in the data-to-simulation ratio for different pseudorapidity ranges of the jet, the measurement of the scaling factors is only done in bins of  $|\eta^{\text{1st jet}}|$ .

How to adjust finally the jet transverse-momentum resolution in simulation to the measured resolution in data is well described in [14].

## 4.1 Validation of the method

The method is validated with simulated events. The bias is shown in Fig. 4.8 for the barrel region. It is evaluated as the ratio of the predicted intrinsic resolution by fitting Eq. (4.5) with  $q$  fixed to the value obtained by Eq. (4.4) over the intrinsic resolution directly obtained from the intrinsic response distribution  $p_T^{\text{reco. jet}}/p_T^{\text{gen. jet}}$ . The result is in good agreement with the expectation to better than 5% above 100 GeV and better

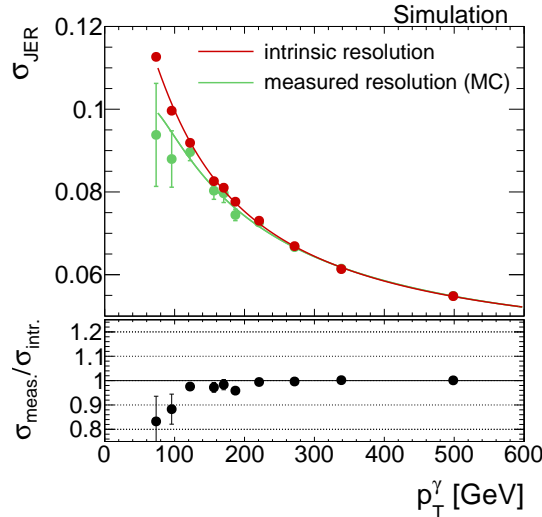


Figure 4.8: Consistency check of the method: Comparison between the “measured” resolution evaluated with Eq. (4.5) and the intrinsic resolution from Eq. (4.3) in simulation.

than 1% above 200 GeV. Only for small  $p_T$ , larger deviations are observed, which are systematically lower than zero (up to 15%).

The residual bias of the method for small  $p_T^\gamma$  is stemming from two effects: First, the binning in  $p_T^\gamma$  and the momentum balance between the photon and the first two jets lead to a dependency of the first jet  $p_T$  on the second jet  $p_T$  and therefore alpha: For a fixed  $p_T^\gamma$ , the  $p_T$  of the first jet gets smaller for larger  $p_T^{2^{\text{nd}} \text{ jet}}$  for events where the second jet is in the leading jet hemisphere (see Fig. 4.3), leading to a dependency of  $p_T^{1^{\text{st}} \text{ jet}} \propto -p_T^{2^{\text{nd}} \text{ jet}}$ . This effect is directly opposite for events with a second jet in the photon hemisphere. In these events, the first jet  $p_T$  gets larger for larger  $p_T^{2^{\text{nd}} \text{ jet}}$  and thus  $p_T^{1^{\text{st}} \text{ jet}} \propto p_T^{2^{\text{nd}} \text{ jet}}$  for fixed  $p_T^\gamma$ . As the resolution of the jet improves with higher jet  $p_T$  (see Fig. 4.7), a dependency of the leading jet  $p_T$  on the second jet  $p_T$  directly leads to a dependency of the intrinsic resolution on the second jet  $p_T$ . In principle, as the effect is opposite for events in the different hemispheres, it should cancel out, when taking the weighted mean of the two hemisphere resolutions. But as the topology of a second jet in the leading jet hemisphere is much more frequent, a residual upward trend in the intrinsic resolution vs.  $\alpha$  is conserved.

The second source of the residual bias arises from the alpha definition  $\alpha = p_T^{2^{\text{nd}} \text{ jet}}/p_T^\gamma$ . Because of the inclusion of  $p_T^\gamma$  in  $\alpha$  with  $\alpha \propto 1/p_T^\gamma$ , the high photon  $p_T$  events accumulate in the low alpha regions. As the selected events are almost balanced, a high  $p_T^\gamma$  is associated with a high jet  $p_T$ , thus also the high jet  $p_T$  events accumulate in the low alpha bins, leading to an upward trend in the intrinsic resolution vs.  $\alpha$ . This behaviour can be seen in the intrinsic resolution in Fig. 4.5, where a small increase of the resolution to high  $\alpha$  can be seen. By fitting a horizontal line to the intrinsic resolution, this effect is averaged out. But the measured resolution with an additional free parameter can adopt this increase and result, therefore, in a y-intercept which is too small. For high photon  $p_T$  bins, this effect is less pronounced, as the slope of  $\text{JER}(p_T^\gamma)$  (see Fig. 4.5) flattens out.

However, this is not of concern here, because the results of the measurement will be presented as resolution scaling factors  $\rho_{\text{res}}$ , defined as the resolution measured in data divided by the resolution measured in Monte Carlo simulation (MC)  $\rho_{\text{res}} = \sigma_{\text{JER}}^{\text{data}}/\sigma_{\text{JER}}^{\text{MC}}$ . Hence, a possible bias in the separate resolution measurements for data and simulation should cancel out. To prove this hypothesis, the simulated dataset is smeared with input values  $\rho_{\text{res}} = 1.1$  in all  $|\eta^{1^{\text{st}} \text{ jet}}|$  bins. As done to determine the data-to-simulation ratio, the relative difference of the resolution measured in the smeared and in the non-smeared dataset is fitted with a constant over the photon  $p_T$  range. The resulting scaling factors  $\rho_{\text{res}}$  should reproduce the input value of  $\rho_{\text{res}} = 1.1$ .

In Fig. 4.9, the comparison of the input and output values is shown. In all  $|\eta^{1^{\text{st}} \text{ jet}}|$  bins, the measurement of the scaling factors reproduces the input factors within the statistical

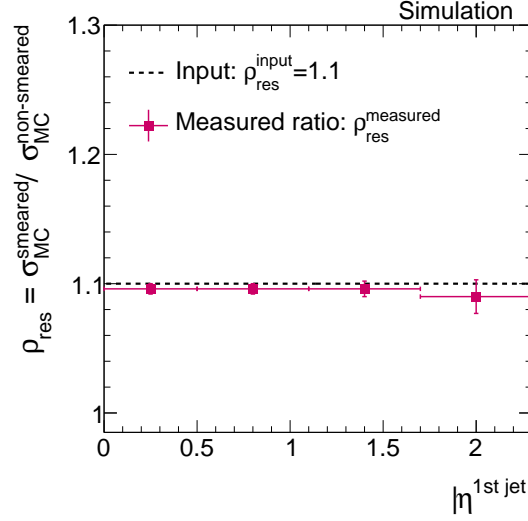


Figure 4.9: Comparison of the resolution ratio  $\sigma_{\text{JER}}^{\text{smeared MC}} / \sigma_{\text{JER}}^{\text{non-smeared MC}}$  measured in simulated events with the input smearing factor  $\rho_{\text{res}} = 1.1$  in all four  $|\eta^{1\text{st jet}}|$  bins.

uncertainties. The deviation of the measured scaling factors to the input value is less than 0.9% in all four  $|\eta^{1\text{st jet}}|$  bins. Thus, the method is expected to hold also for the determination of the data-to-simulation ratio.

After the characterisation and estimation of the associated systematic uncertainties of the jet transverse-momentum resolution measurement with  $\gamma + \text{jet}$  events, the results of the measurement on 8 TeV data will be presented.

## 5 Systematic uncertainties

Many systematic uncertainties of the jet transverse-momentum resolution measurement cancel out when focusing on the data-to-simulation ratio  $\sigma_{\text{JER}}^{\text{data}} / \sigma_{\text{JER}}^{\text{MC}}$ . In the following subsections, only uncertainties relevant for this ratio will be discussed.

For the final uncertainty, the single uncertainties are added in quadrature, resulting in relative uncertainties between 2.3% to 6.3% for the lowest and highest  $|\eta^{1\text{st jet}}|$  bin, respectively.

An overview of all systematic uncertainties can be found in Table 5.1.

Table 5.1: All relative systematic uncertainties on the data-to-simulation ratio  $\sigma_{\text{JER}}^{\text{data}}/\sigma_{\text{JER}}^{\text{MC}}$  listed by sources for the different  $|\eta^{\text{jet}}|$  bins.

	$ \eta^{\text{jet}} $			
	0.0 - 0.5	0.5 - 1.1	1.1 - 1.7	1.7 - 2.3
<b>Multijet contamination</b>	+2.0%	+2.0%	+2.3%	+2.5%
	-2.0%	-2.0%	-2.3%	-2.5%
<b>Flavor uncertainty</b>	+0.9%	+0.9%	+0.8%	+0.6%
	-0.9%	-0.9%	-0.8%	-0.6%
<b>JES uncertainty</b>	+0.6%	+0.6%	+0.6%	+0.7%
	-0.5%	-0.6%	-0.6%	-0.6%
<b>Out-of-Cone showering simulation</b>	+0.5%	+2.8%	+3.6%	+5.7%
	-0.5%	-2.8%	-3.6%	-5.7%
<b>PU uncertainty</b>	+0.1%	+0.1%	+0.1%	+0.2%
	-0.1%	-0.1%	-0.2%	-0.2%
<b>Total</b>	+2.3%	+3.6%	+4.4%	+6.3%
	-2.3%	-3.6%	-4.4%	-6.3%

## Uncertainty on the contamination with QCD-multijet events

Although the photon selection is very strict (see Section 3.3), due to the huge multijet cross section, a countable fraction of dijet events can survive the selection with a jet misidentified as photon. This happens, when e. g. a jet hadronises to a  $\pi^0$  that decays to two photons which is sometimes not distinguishable from the isolated photon of a  $\gamma$  + jet event for the detector.

In principle, those dijet events have the same topology as  $\gamma$  + jet events. The two leading jets are also balanced apart from initial and final state radiation. Therefore, the method is generally expected to hold. A worsening of the resolution because of background contamination is only expected due to the mismeasurement of the  $p_{\text{T}}$  of the jet misidentified as photon, because only the energy of the  $\pi^0$  is counted and not the full energy. Another aspect is the different flavor composition of a QCD-multijet sample. Due to the different production mechanism, QCD-dijets are predominantly initiated by gluons while the leading jet in  $\gamma$  + jet events often stems from a light quark, cf. Fig. 2.2. The number of

particles after hadronisation is typically larger for gluon jets, hence the single particles are less energetic and out-of-cone showering is more pronounced. Since in this analysis the residual imbalance  $q$  is taken from the simulation where only a  $\gamma$ +jet sample is considered, it is not expected to accurately describe the residual imbalance in the data sample where also dijet events occur.

To investigate the impact of QCD-multijet contamination, a QCD-multijet sample, enriched in jets with a large electromagnetic fraction, is added to the  $\gamma$ +jet sample and weighted according to the cross section. Since the QCD-multijet sample has very large event weights leading to high statistical uncertainties in the measured jet transverse-momentum resolution, some selection criteria ( $\alpha < 0.4$  and  $\Delta\Phi > 2.7$ ) are relaxed in order to increase the statistical precision of the uncertainty estimation. Additionally, a rougher binning in  $\alpha$ ,  $p_T^\gamma$  and  $|\eta^{1\text{st jet}}|$  is applied.

The residual imbalance  $q$  of the resolution measurement including the QCD-multijet sample is fixed to the residual imbalance determined from the  $\gamma$ +jet only analysis to account for a possible error in the evaluation of the  $\sigma_{\text{JER}}^{\text{data}}/\sigma_{\text{JER}}^{\text{MC}}$  ratio where data is only compared to a  $\gamma$ +jet sample.

In Fig. 5.1, the resolution measured when using both the  $\gamma$ +jet and the QCD-multijet sample is compared to the resolution measured only with the  $\gamma$ +jet sample. It can be seen, that the resolution is worse for low  $p_T^\gamma$  when considering QCD-multijet contamination.

The impact on the data-to-simulation ratio is estimated by adding the QCD-multijet sample on top of the  $\gamma$ +jet sample and redoing the evaluation of the scaling factors.

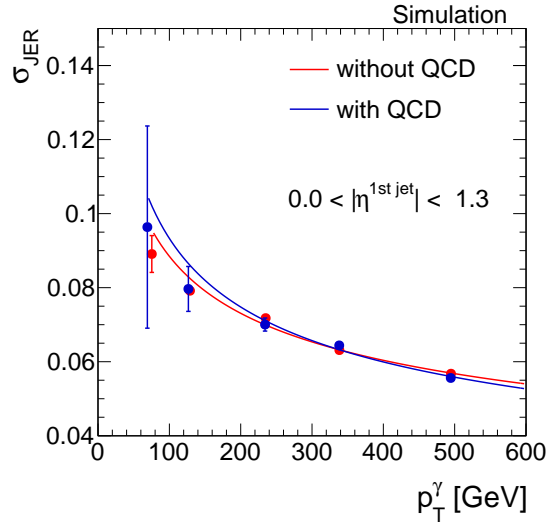


Figure 5.1: The jet transverse-momentum resolution measured in simulation for  $|\eta^{1\text{st jet}}| < 1.3$  with (blue) and without (green) a QCD-multijet sample added to the  $\gamma$ +jet sample.



The resulting uncertainties vary between 2.0 – 2.5% for the different  $|\eta^{1\text{st jet}}|$  regions (cf. Table 5.1).

## Uncertainty on the flavor composition in simulation

A possible difference among the resolution of different jet flavors (caused by e.g. more pronounced out-of-cone showering of gluon jets) should in principle not play a role for the data-to-simulation scaling factors  $\rho_{\text{res}}$  as long as the flavor composition of the data and simulation samples is the same.

To account for possible discrepancies in the flavor composition between data and simulation, the gluon and quark flavor fractions of the simulated sample are varied by 10%.

The composition in the simulated PYTHIA  $\gamma + \text{jet}$  sample is around 60% light quarks and 20% to 35% gluons (see Fig. 5.2). The missing fraction is mainly made up out of charm quarks.

To estimate the effect of different flavour compositions, the resolution in simulation is separately evaluated for quarks ( $\sigma_{\text{JER}}^{\text{quarks}}$ ) and gluons ( $\sigma_{\text{JER}}^{\text{gluons}}$ ). There are various definitions used in the CMS collaboration how to assign the underlying generator-level quark/gluon flavor to a jet. In this measurement the so-called “algorithmic” flavor definition is used which classifies b- or c-jets from gluon splitting as b- or c-quarks (see Appendix A.3 for more details on this definition).

Figure 5.3 shows the differences in the resolution for all flavors separately for  $|\eta^{1\text{st jet}}| < 1.3$ . The resolution for gluon and light quark jets is comparable for small  $p_T^\gamma$  and gets larger

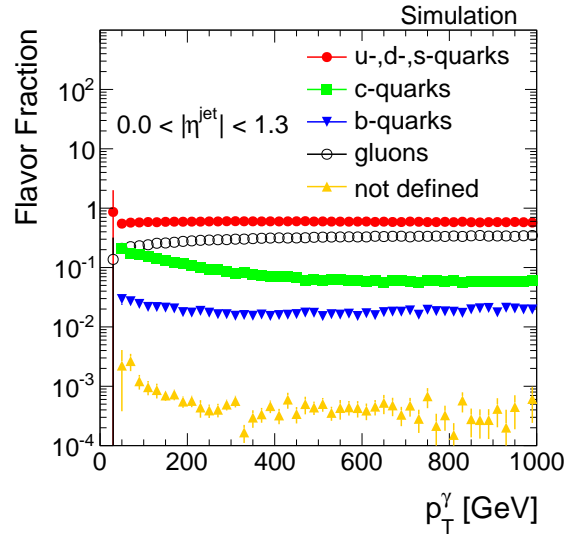


Figure 5.2: The flavor composition in the  $\gamma + \text{jet}$  sample in the barrel region of the detector. The “algorithmic” flavor definition is used (see Appendix A.3 for more details).

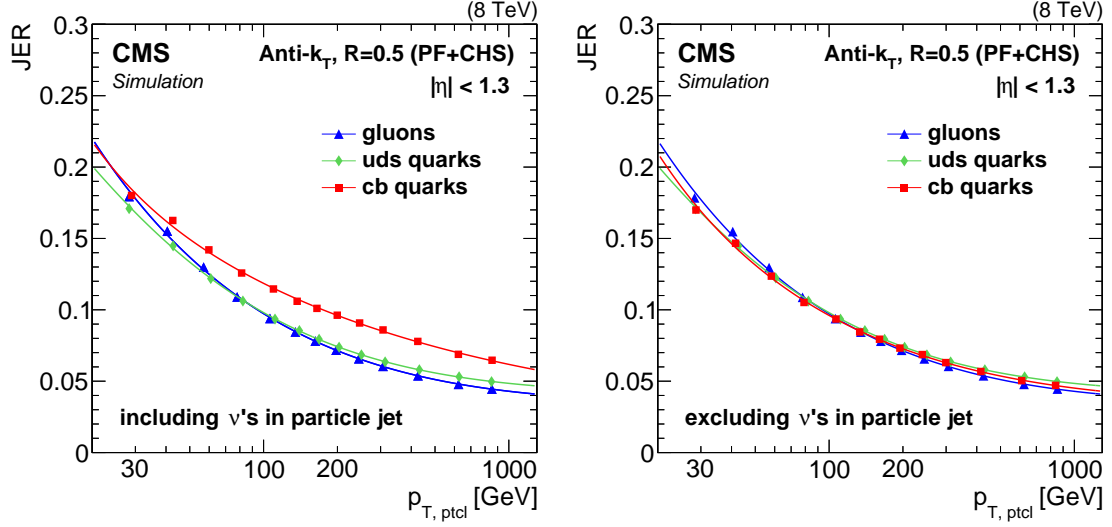


Figure 5.3: The intrinsic resolution  $\sigma_{\text{intr.}}$  for  $|\eta^{1\text{st jet}}| < 1.3$  for different jet flavors with (left) and without (right) including the neutrinos in the generator-level jet. Here, JER refers to  $\sigma_{\text{intr.}}$ , and  $p_{T,\text{ptcl}}$  to the generator-level jet  $p_T$ .

for high  $p_T^\gamma$ . Since the transverse momentum of neutrinos is counted into the generator-level jet  $p_T$ , the resolution of charm and bottom quarks is therefore shifted to larger resolution values (left part of Fig. 5.3). This is not the case, if the neutrino  $p_T$  is not added to the generator-level jet  $p_T$ , as can be seen in Fig 5.3 (right). However, for the here presented measurement it does not play a role whether the neutrino  $p_T$  is or is not added to the generator-level jet  $p_T$ , because in case it is not included into the intrinsic response the long right tail of the response function for b- and c-quarks is then transferred to the imbalance response. Thus, the right tail of b- and c-quarks does anyway enter the jet transverse-momentum resolution measurement with  $\gamma + \text{jet}$  events, either in the intrinsic response or in the imbalance response.

The weighted mean of the quark and the gluon resolution is then taken to estimate the resolution for different flavor compositions, such that the flavor fractions are varied by 10%. Finally, the constant fit to the data-to-simulation ratio  $\sigma_{\text{JER}}^{\text{data}}/\sigma_{\text{JER}}^{\text{MC}}$  is reevaluated, leading to a final systematic uncertainty between 0.6 – 0.9%.

## Uncertainty on the simulation of out-of-cone showering

Another source of uncertainty is the use of information from Monte Carlo simulation by determining the residual imbalance  $q$  from the simulated  $\gamma + \text{jet}$  sample (Eq. (4.5)).

Since it cannot be expected that out-of-cone showering is well modelled in simulation, possible differences between real and simulated out-of-cone showering are estimated by

the evaluation of the ratio  $\sigma_{\text{JER}}^{\text{data}}/\sigma_{\text{JER}}^{\text{MC}}$  using different jet radii of the jet reconstruction algorithm.

For the primary analysis, jets reconstructed by the Anti- $k_t$  algorithm with a radius of  $R = 0.5$  are used (AK5-jets). In order to evaluate the systematic uncertainty on the out-of-cone showering simulation, the measurement of  $\rho_{\text{res}}$  redone with jets reconstructed with a jet radius of  $R = 0.7$  (AK7-jets).

The data-to-simulation ratio is in all  $|\eta^{1^{\text{st}} \text{ jet}}|$  bins larger for AK7-jets, resulting in uncertainties between 0.5 – 5.7%. The uncertainty on the simulation of out-of-cone showering is thereby the largest systematic uncertainty of this measurement.

## Uncertainty on the jet energy scale

Another source of uncertainty arises from the correction of the jet energy scale. The transverse momentum of each jet is corrected in order to have uniform response over the full  $\eta^{\text{jet}}$ , and  $p_{\text{T}}^{\text{jet}}$  range [15]. In simulation, it is additionally corrected to account for data-simulation differences. The latter correction can be a important for the evaluation of the data-to-simulation ratio  $\rho_{\text{res}}$ . Thus, the uncertainties on the correction factors that are only applied to the simulated samples are varied up and down within their  $1\sigma$ -uncertainties.

The effect of the jet  $p_{\text{T}}$  variation on the data-to-simulation ratio is of minor importance and range between 0.5 – 0.7%.

## Uncertainty on the pileup reweighting

Finally, an uncertainty due to the adjustment of the simulated events to the pileup distribution in data is evaluated.

To account for this uncertainty, the effect of a 5.0% up- and downward variation of the minimum-bias cross section (69.4 mb) on the resolution is evaluated, following the recommended procedure from [16]. The resulting uncertainties are almost negligible and range between 0.1 – 0.2%.

# 6 Results

The data-to-simulation resolution scaling factors  $\rho_{\text{res}} = \sigma_{\text{JER}}^{\text{data}}/\sigma_{\text{JER}}^{\text{MC}}$  are determined in  $19.7 \text{ fb}^{-1}$  of pp collision data at  $\sqrt{s} = 8 \text{ TeV}$  with the methodology described in Chapter 4. In each  $\alpha$ -,  $p_{\text{T}}^{\gamma}$ - and  $|\eta^{1^{\text{st}} \text{ jet}}|$ -bin, the width of the 99% truncated response histogram is determined in simulation and data. Afterwards, the extrapolation to zero additional jet

activity is carried out, by fixing the imbalance  $q$  in simulation and in data to the value extracted from the imbalance extrapolation in simulation. Exemplary extrapolations for the imbalance and the total resolution in data and simulation are shown in Fig. 6.1.

The full set for each  $p_T^\gamma$  and  $|\eta^{1\text{st jet}}|$  bin can be found in Appendix A.4.

Finally, the extracted resolutions in data and simulation in every  $p_T^\gamma$  bin are divided and a horizontal fit is applied to this ratio

$$\frac{\sigma_{\text{JER}}^{\text{data}}}{\sigma_{\text{JER}}^{\text{MC}}}(p_T^\gamma).$$

In Fig. 6.2, the results for all four  $|\eta^{1\text{st jet}}|$ -ranges are depicted. The  $\chi^2/\text{NDF}$ -values for the four fits vary between 0.23 and 2.53. Thus, a horizontal fit is justified, and one value for every  $|\eta^{1\text{st jet}}|$ -bin will be reported.

All fit results are greater than one which means that the resolution in data is in all bins worse compared to the resolution in simulation. The values of the fits range from 1.067 (for the first  $\eta^{\text{jet}}$ -bin) to 1.199 (for the last  $\eta^{\text{jet}}$ -bin).

The systematic uncertainties are evaluated as described in the previous chapter. The single uncertainties are taken as upper and lower boundary of the 68% uncertainty band and are added in quadrature to get the total systematic uncertainty. Table 6.1 summarises

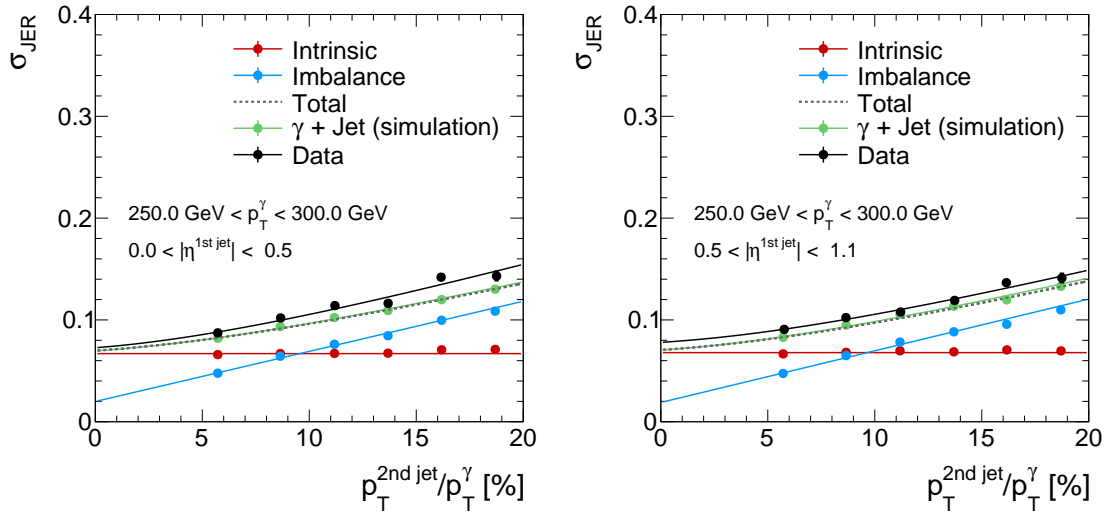


Figure 6.1: Two examples of the alpha dependency of the measured jet transverse-momentum resolution in data (black dots), in simulation (green dots) and of the intrinsic (red dots) and the imbalance (blue dots) part of the resolution in simulated events. All resolutions are fitted with the corresponding functions introduced in Chapter 4 (Eqs. (4.3)- (4.5)). The total resolution (grey dotted line) is the addition in quadrature of the imbalance (blue line) and the intrinsic (red line) fit functions.

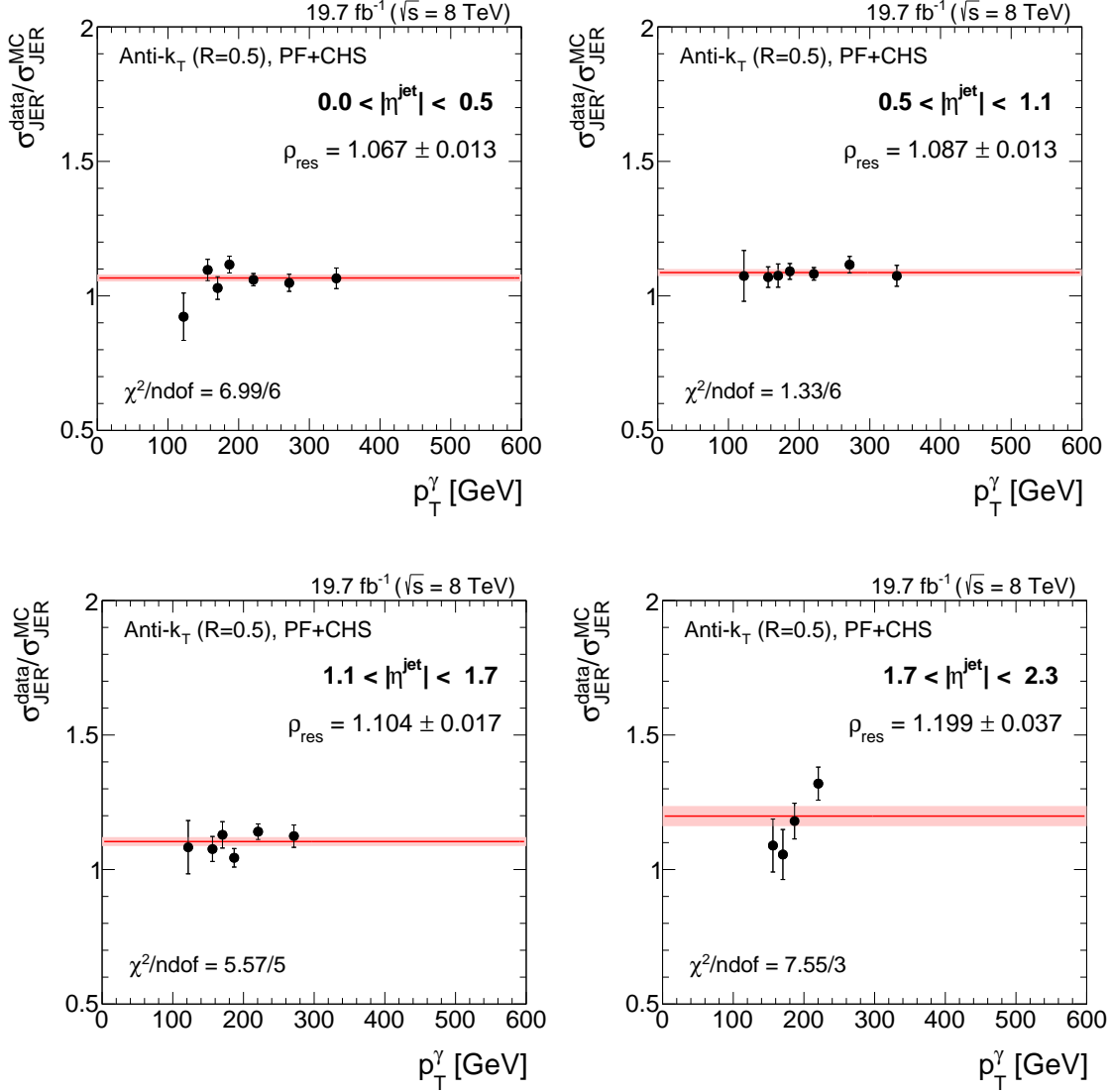


Figure 6.2: Data-to-simulation resolution ratios (black dots), fitted with a horizontal line (red line) for four different  $|\eta^{\text{jet}}|$ -ranges. The fit uncertainties are depicted with light red error bands.

the data-to-simulation ratio results determined with data collected during the year 2012 with their statistical and systematic uncertainties. The visualised result can be found in Fig. 6.3.

Though the  $\gamma + \text{jet}$  analysis is known to be capable to produce highly precise results, the systematic uncertainties are still dominating. This is mainly caused by the uncertainty on the simulation of out-of-cone showering. This uncertainty, however, is limited because of the statistical precision of the  $\gamma + \text{jet}$  dataset. Thus, this analysis is mainly statistically

Table 6.1: Data-to-simulation resolution scaling factors  $\rho_{\text{res}}$  with statistical and systematic uncertainties.

$ \eta^{\text{jet}} $	$\rho_{\text{res}}$	stat.	sys.
0.0 – 0.5	1.067	$\pm 0.013$	$+0.025$ $-0.024$
0.5 – 1.1	1.087	$\pm 0.013$	$+0.039$ $-0.039$
1.1 – 1.7	1.104	$\pm 0.017$	$+0.049$ $-0.049$
1.7 – 2.3	1.199	$\pm 0.037$	$+0.075$ $-0.075$

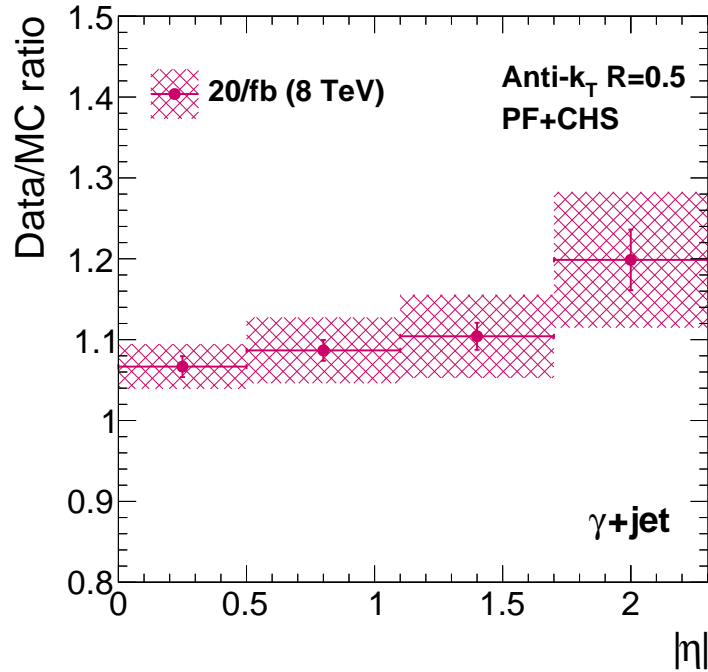


Figure 6.3: The measured data-to-simulation resolution ratio in  $\gamma + \text{jet}$  events using data recorded in the year 2012. The red band depicts the total uncertainty whereas the error bars show the statistical uncertainty only.

limited because of the limited number of events recorded in 2012 at the CMS detector. The number of simulated events is roughly eight times larger.

## 6.1 Comparison to 2011 measurements

A comparison of the data-to-simulation resolution scaling factors between this analysis and the results of 2011 which were determined from a dijet data sample [?] can be found in Fig. 6.4.

The black dots show the  $\sigma_{\text{JER}}^{\text{data}}/\sigma_{\text{JER}}^{\text{MC}}$  scale factors of the 2011 analysis with the grey band representing the statistical and systematic uncertainties added in quadrature while the magenta dots and the magenta band are the 2012 central values with their total uncertainties. (FIXME: is this correct).

It can be seen, that throughout the whole  $\eta^{\text{jet}}$ -range the data-to-simulation are systematically larger for the result in 2011.

Comparing the precision of both measurements, the  $\gamma$ +jet analysis is for all  $\eta$ -bins more precise than the analysis done with dijet events. This is due to the smaller systematic uncertainties of the  $\gamma$ +jet analysis which compensates for the better statistical precision of the QCD-multijet sample due to the large cross section.

BLABLABLA!!!

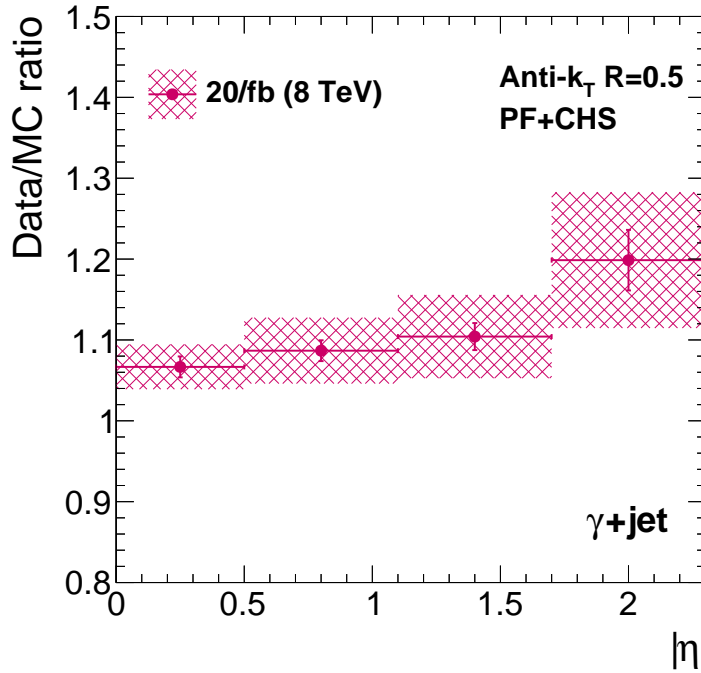


Figure 6.4: FIXME: Other plot here.

## **6.2 Comparison to dijet measurement**



## 7 Discussion and conclusion

A first measurement of the resolution ratio  $\frac{\text{JER}^{\text{data}}}{\text{JER}^{\text{MC}}}$  using  $\gamma + \text{jet}$  events with  $19.7 \text{ fb}^{-1}$  pp collision data at  $\sqrt{s} = 8 \text{ TeV}$  collected in 2012 at the CMS detector has been presented. For this purpose, the methodology introduced in [?] was further developed to take account of the double peak structure when applying an exclusive binning in the variable  $\alpha$  that measures the additional jet activity in the event.

The resolution in data was found to be systematically larger than in the simulation throughout the investigated  $\eta^{\text{jet}}$  plane. A possible  $p_{\text{T}}^{\gamma}$  dependence of the resolution scale factors was not visible. Thus, the ratio has been parametrised with a constant per  $\eta^{\text{jet}}$  bin.

The relative difference of the data resolution ranges from  $\sim 7\%$  to  $\sim 20\%$  for  $0.0 < |\eta^{\text{jet}}| < 0.5$  and  $1.7 < |\eta^{\text{jet}}| < 2.3$ , respectively, with total statistical and systematic uncertainties between 3% and 8%.

- Repeat results
- cross-check analysis
- Outlook



## A Measurement of the jet transverse momentum resolution

### A.1 Pileup reweighting

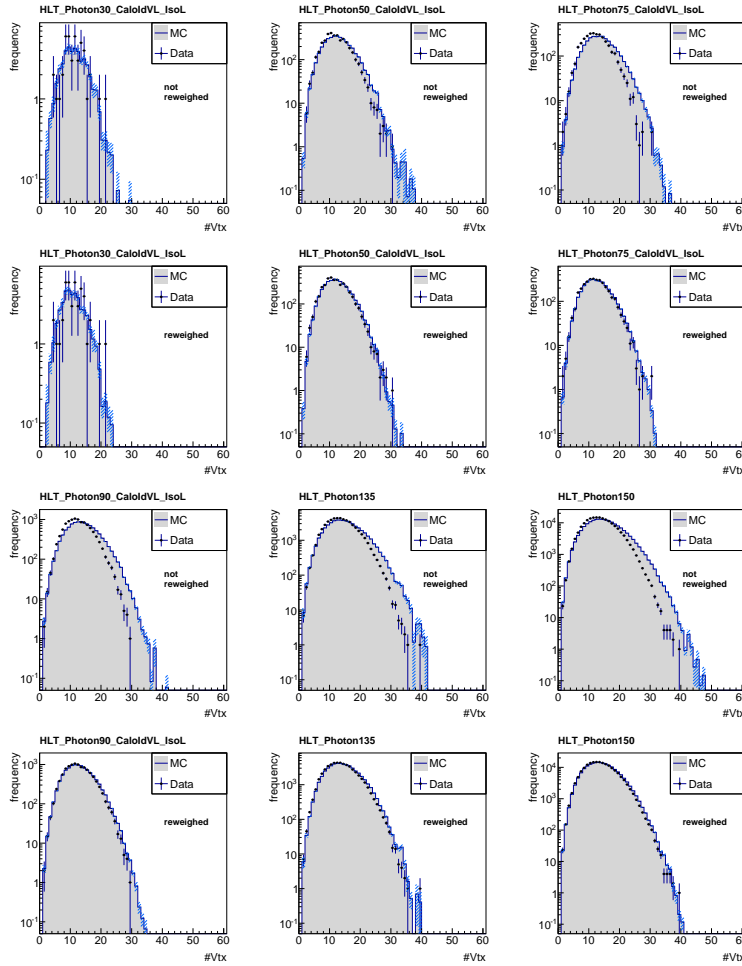


Figure A.1: The number of primary vertices in data and simulation before (1st row) and after (2nd row) pileup reweighting for  $36 \text{ GeV} < p_T^\gamma < 60 \text{ GeV}$  (left),  $60 \text{ GeV} < p_T^\gamma < 88 \text{ GeV}$  (middle), and  $88 \text{ GeV} < p_T^\gamma < 105 \text{ GeV}$  (right) and the number of primary vertices in data and simulation before (3rd row) and after (4th row) pileup reweighting for  $105 \text{ GeV} < p_T^\gamma < 149 \text{ GeV}$  (left),  $149 \text{ GeV} < p_T^\gamma < 165 \text{ GeV}$  (middle), and  $165 \text{ GeV} < p_T^\gamma$  (right).

## A.2 Summary of all selection requirements

Table A.1: Summary of all selection criteria for the measurements of the jet transverse-momentum resolution with  $\gamma + \text{jet}$  events.

One jet with	$p_T > 10 \text{ GeV}$ Neutral hadron fraction $< 0.90$ Neutral electromagnetic fraction $< 0.90$ Number of constituents $> 1$ Charged hadron fraction $> 0$ Charged hadron multiplicity $> 0$
One photon with	$p_T > 22 \text{ GeV}$ $ \eta  < 1.3$ $\frac{H}{E} < 0.05$ $\sigma_{in\eta} < 0.013$ ECAL isolation $< 4.2 \text{ GeV} + 0.0060 \cdot p_T^\gamma$ HCAL isolation $< 2.2 \text{ GeV} + 0.0025 \cdot p_T^\gamma$ Track Isolation $< 2.0 \text{ GeV} + 0.0010 \cdot p_T^\gamma$ Pixel seed veto
Event-based selection	$p_T^{2^{\text{nd}} \text{ jet}} > 10 \text{ GeV}$ $\frac{p_T^{2^{\text{nd}} \text{ jet}}}{p_T^\gamma} < 0.20$ $\Delta\Phi(1^{\text{st}} \text{ jet}, \gamma) > 2.95$

## A.3 Generator-level jet flavor definition

The algorithmic flavor definition uses the following discrimination:

- Try to find the parton that most likely determines the properties of the jet and assign that flavor as true flavor

- Here, the “final state” partons (after showering, radiation) are analyzed (also within  $\Delta R < 0.3$  of reconstructed jet cone)
- Jets from radiation are matched with full efficiency
- If there is a b/c within the jet cone: label as b/c
- Otherwise: assign flavor of the hardest parton

## A.4 Extrapolation plots

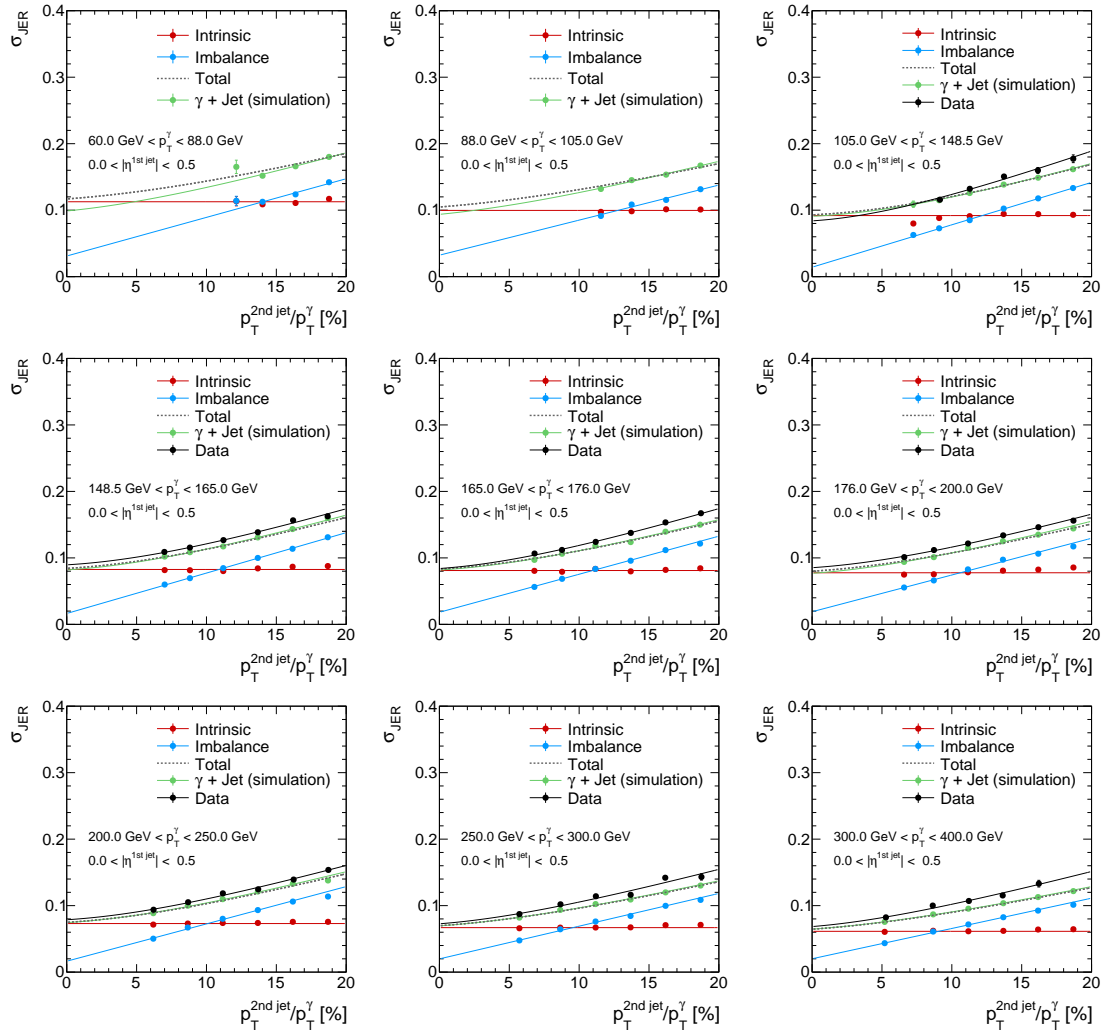


Figure A.2:  $\sigma_{\text{JER}}(\alpha)$  of the intrinsic, imbalance and total resolution in simulation and the resolution measured in data for all  $|\eta^{\text{1st jet}}|$  and  $p_T^\gamma$  bins.

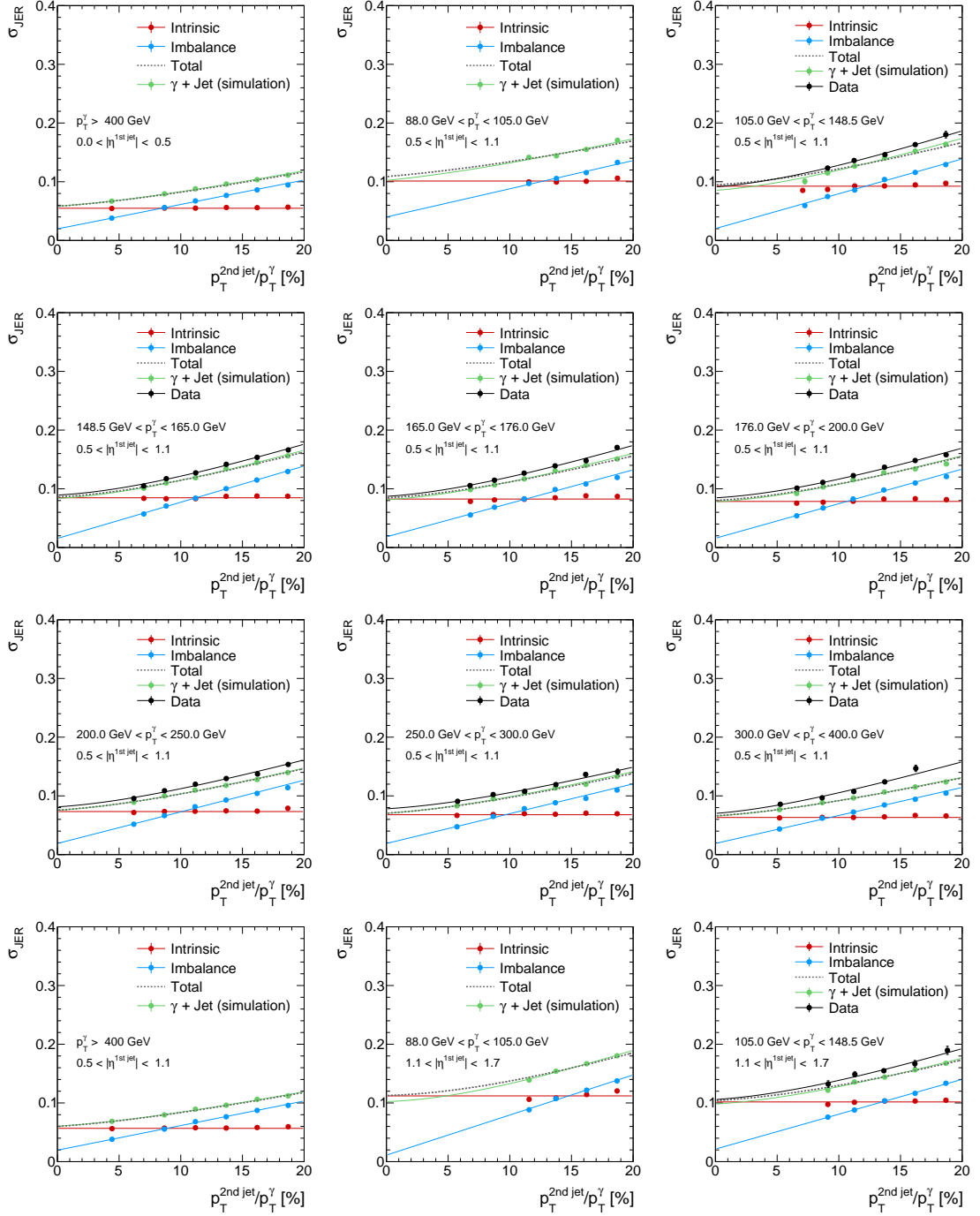


Figure A.3: Continued from Fig. A.2:  $\sigma_{\text{JER}}(\alpha)$  of the intrinsic, imbalance and total resolution in simulation and the resolution measured in data for all  $|\eta^{1\text{st jet}}|$  and  $p_T^\gamma$  bins.

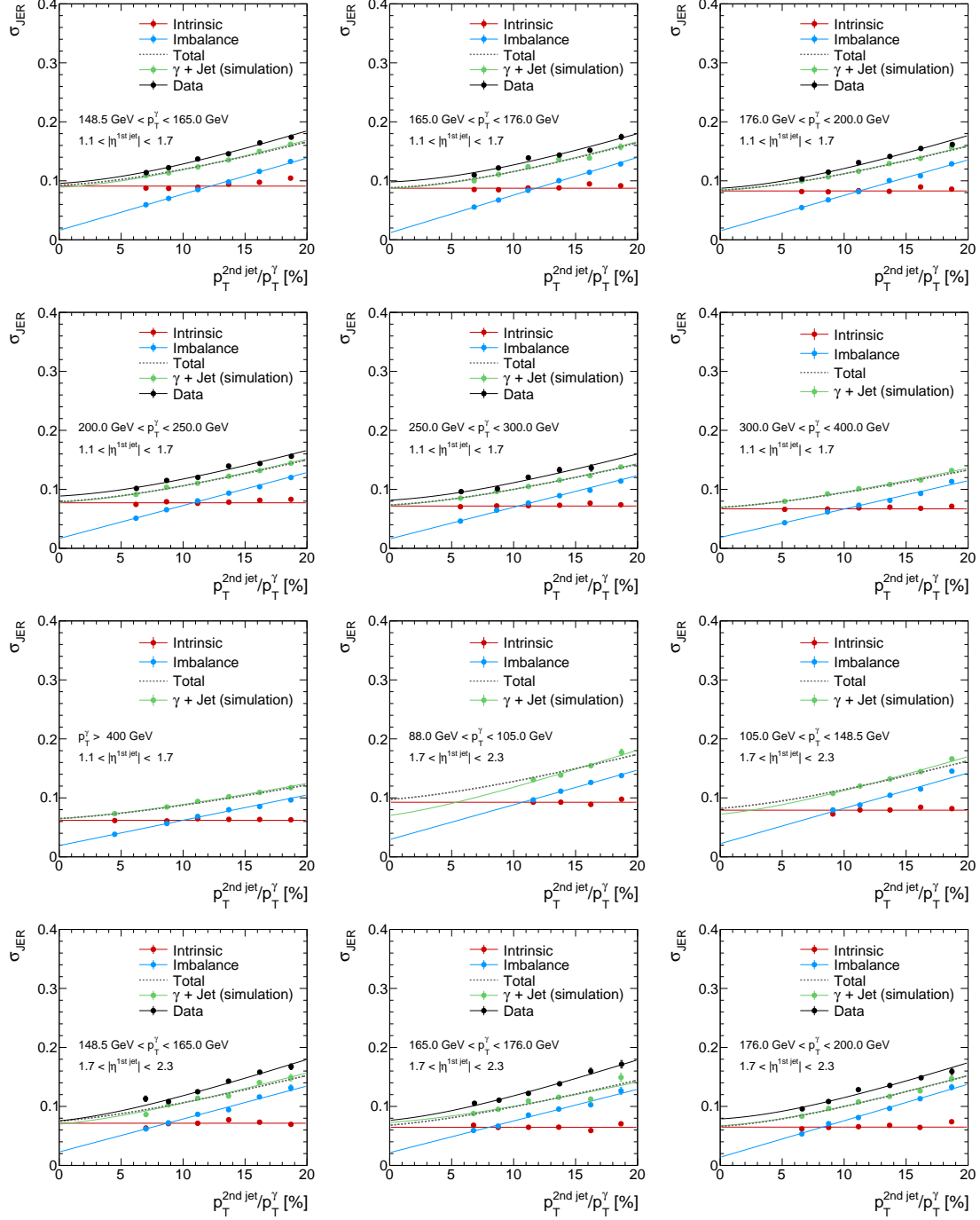


Figure A.4: Continued from Fig. A.3:  $\sigma_{\text{JER}}(\alpha)$  of the intrinsic, imbalance and total resolution in simulation and the resolution measured in data for all  $|\eta^{1\text{st jet}}|$  and  $p_T^\gamma$  bins.

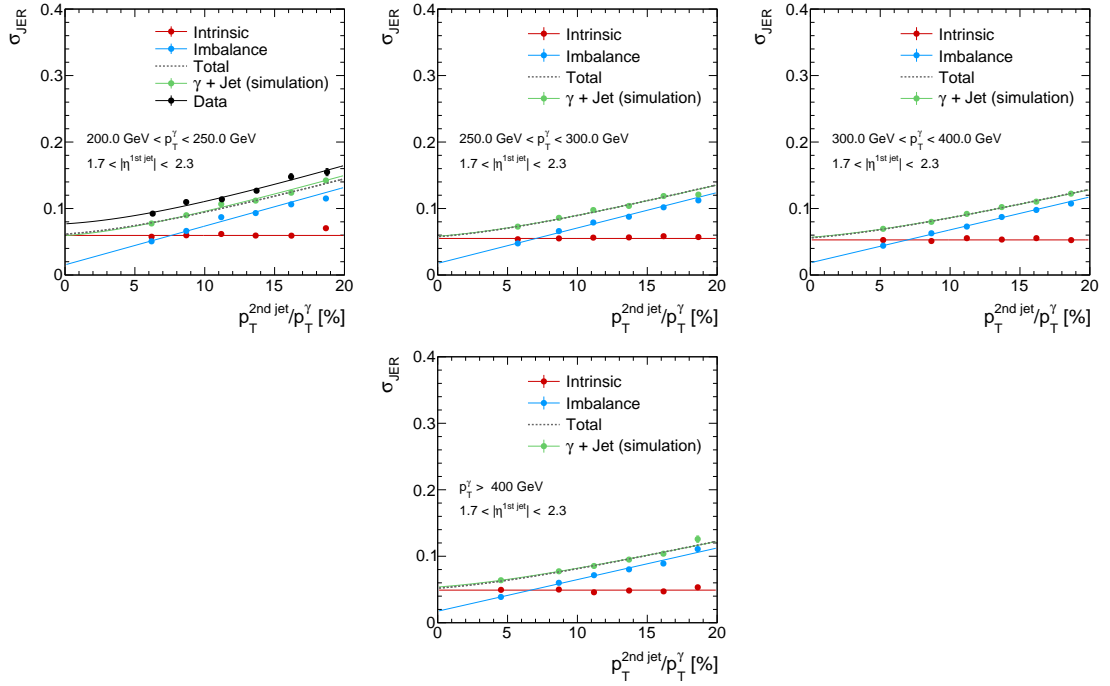


Figure A.5: Continued from Fig. A.4:  $\sigma_{\text{JER}}(\alpha)$  of the intrinsic, imbalance and total resolution in simulation and the resolution measured in data for all  $|\eta^{1\text{st jet}}|$  and  $p_T^\gamma$  bins.



## Bibliography

- [1] CMS Collaboration, “Measurements of differential dijet cross section in proton-proton collisions at  $\sqrt{s} = 8$  TeV with the CMS detector”, *CMS Physics Analysis Summary* **CMS-PAS-SMP-14-002** (2014).
- [2] CMS Collaboration, “Measurement of the differential cross section for top quark pair production in pp collisions at  $\sqrt{s} = 8$  TeV”, *Eur. Phys. J.* **C75** (2015), no. 11, 542, [arXiv:1505.04480](#). doi:10.1140/epjc/s10052-015-3709-x.
- [3] CMS Collaboration, “Search for new physics in the multijet and missing transverse momentum final state in proton-proton collisions at  $\sqrt{s} = 8$  TeV”, *JHEP* **06** (2014) 055, [arXiv:1402.4770](#). doi:10.1007/JHEP06(2014)055.
- [4] CMS Collaboration, “Searches for Supersymmetry using the  $M_{T2}$  Variable in Hadronic Events Produced in pp Collisions at 8 TeV”, *JHEP* **05** (2015) 078, [arXiv:1502.04358](#). doi:10.1007/JHEP05(2015)078.
- [5] CMS Collaboration, “Search for supersymmetry in hadronic final states with missing transverse energy using the variables  $\alpha_T$  and b-quark multiplicity in pp collisions at  $\sqrt{s} = 8$  TeV”, *Eur. Phys. J.* **C73** (2013), no. 9, 2568, [arXiv:1303.2985](#). doi:10.1140/epjc/s10052-013-2568-6.
- [6] CMS Collaboration, “Determination of Jet Energy Calibration and Transverse Momentum Resolution in CMS”, *JINST* **6** (2011) P11002, [arXiv:1107.4277](#). doi:10.1088/1748-0221/6/11/P11002.
- [7] CMS Collaboration, “Jet Energy Resolution in CMS at  $\sqrt{s} = 7$  TeV”, *CMS Physics Analysis Summary* **CMS-PAS-JME-10-014** (2011).
- [8] CMS Collaboration, “Performance of Photon Reconstruction and Identification with the CMS Detector in Proton-Proton Collisions at  $\sqrt{s} = 8$  TeV”, *JINST* **10** (2015), no. 08, P08010, [arXiv:1502.02702](#). doi:10.1088/1748-0221/10/08/P08010.
- [9] CMS Collaboration, CMS Collaboration, “Particle-Flow Event Reconstruction in CMS and Performance for Jets, Taus, and MET”, CMS Physics Analysis Summary **CMS-PAS-PFT-09-001**, 2009.

- 
- [10] M. Cacciari, G. P. Salam, and G. Soyez, “The anti- $k_t$  jet clustering algorithm”, *JHEP* **04** (2008) 063, [arXiv:0802.1189](#). doi:10.1088/1126-6708/2008/04/063.
  - [11] N. Odell, “PF Jet ID Recommendation”.  
[https://indico.cern.ch/event/89919/contribution/0/attachments/1091238/1556772/PF\\_JET\\_ID\\_Recommendation.pdf](https://indico.cern.ch/event/89919/contribution/0/attachments/1091238/1556772/PF_JET_ID_Recommendation.pdf), April, 2010.
  - [12] N. Saoulidou and E. Tziaferi, “Performance of the Particle-Flow jet identification criteria using proton-proton collisions at  $\sqrt{s} = 8$  TeV”, *CMS Analysis Note CMS-AN-14-227* (2014). Internal documentation.
  - [13] CMS Collaboration, “Isolated Photon Reconstruction and Identification at  $\sqrt{s} = 7$  TeV”, *CMS Physics Analysis Summary CMS-PAS-EGM-10-006* (2011).
  - [14] M. Schröder, “Quality of jet measurements and impact on a search for new physics at CMS”. PhD thesis, Hamburg U., 2012.
  - [15] CMS Collaboration, “Jet Energy Scale and Resolution in the CMS Experiment”, *CMS Physics Analysis Summary CMS-PAS-JME-13-004* (2015).
  - [16] CMS Collaboration, “Pileup Reweighting”, *Internal CMS Wiki* (2011).  
<https://twiki.cern.ch/twiki/bin/viewauth/CMS/PileupReweighting>.

